Ferroelectric domain engineering using structural defect ordering

Elzbieta Gradauskaite[1,*], Kasper A. Hunnestad[2], Quintin N. Meier[3], Dennis Meier[2], Morgan Trassin[1,*]

[*]elzbieta.gradauskaite@mat.ethz.ch, morgan.trassin@mat.ethz.ch

[1]*Department of Materials, ETH Zurich, 8093 Zurich, Switzerland*

[2]*Department of Materials Science and Engineering, NTNU, 7491 Trondheim, Norway*

[3]*Univ. Grenoble Alpes, CEA, LITEN, 38054 Grenoble, France*

ABSTRACT

Ferroelectrics have become indispensable in the development of energy-efficient oxide electronics. Their domain state is closely linked to the final device functionality, making domain engineering in technology-compatible thin films of paramount importance. Here we demonstrate the local control of domain formation in two-dimensional epitaxial ferroelectric films using structural defect engineering through the substrate topography. Using a combination of first-principles calculations, atom probe tomography, and scanning probe microscopy, we show that out-of-phase boundaries induced at the substrate step edges combined with local off-stoichiometry trigger the formation of ferroelectric domain walls in the layered ferroelectric $Bi_5FeTi_3O_{15}$ (BFTO) Aurivillius thin films. The substrate treatment and the miscut angle selection allow for precise control of domain size and location in both single layers and multilayer architectures. With this work, we establish a new route for ferroelectric domain

engineering and stabilization of functional domain walls in ultrathin ferroelectric layers.

Ferroic domains, defined as regions with a uniform orientation of the order parameter, define the device functionality in oxide electronics. They can be nucleated, moved, and erased at will.[1–3] In electrically ordered ferroics, i.e., ferroelectrics, emerging device paradigms are based on the manipulation of such domains, including ferroelectric memristors,[4,5] as well as the domain-wall memories[6,7] and nanocircuitry.[8–10] This renders the control of domain formation of uttermost importance for the integration of ferroic oxides into novel nanoscale devices.

Ferroelectric domain engineering traditionally involves the use of strain[11] or electrostatics.[2,12] These approaches enable the control of macroscopic functional properties in thin films, such as the ferroelectric anisotropy,[13,14] the allowed domain states, and their populations,[13,14] as well as the internal structure and properties of the domain walls.[15] Nevertheless, in pristine ferroelectric films, the deterministic nucleation of domains at predefined locations with controlled dimensions on the microscale has remained challenging, hindering the development of ferroelectric nanoscale devices with predetermined functional elements.

Here we demonstrate the controlled ordering of structural defects that drive the predefined nucleation of ferroelectric domains in oxide thin films, using a combination of density-functional theory (DFT) calculations, phase-field simulations, atom probe tomography (APT), and piezoresponse force microscopy (PFM). We employ the substrate steps of (001)-oriented $NdGaO_3$ (NGO) to trigger the formation of out-of-phase boundaries (OPBs) in layered Aurivillius ferroelectric $Bi_5FeTi_3O_{15}$ (BFTO). These structural defects combined with local off-stoichiometry induce pe-

riodic arrays of ferroelectric head-to-head (HH) and tail-to-tail (TT) domain walls in the ultrathin ferroelectric layers. The domain-wall locations are set by the substrate step positions, while the domain size is determined by the substrate miscut angle. Thermal annealing influences the substrate step morphology and defines the domain shape. Going beyond single ferroelectric layers, we exploit the propagation of structural defects in dielectric superlattices to achieve the domain ordering throughout the volume of the multilayer. Thus, we use structural defects in layered ferroelectrics for ferroelectric domain engineering and for the stabilization of nominally charged domain walls. The demonstrated nucleation of domain walls at predefined locations provides additional opportunities for tailoring the electronic responses of functional ferroic systems for the ever-evolving field of oxide electronics.

Out-of-phase boundaries (OPBs) are structural defects in crystals that appear between adjacent regions that are misaligned by a fraction of a unit-cell parameter.[16,17] These defects form spontaneously during synthesis and correspond to perturbations in the lattice inducing local strain fields, creating non-uniform electrostatics and hence affecting the physical properties of the films[18–21] and in some cases even result in the formation of ferroelectric domains.[21,22] This motivates our choice of OPBs as structural defects to be explored for ferroelectric domain engineering. As these structural defects naturally form in layered compounds,[16] we start our investigation in ferroelectric thin films of the layered Aurivillius phase,[23–25] taking BFTO as our model system.

The orthorhombic BFTO unit cell (u.c.) comprises alternating flourite-like $[Bi_2O_2]^{2+}$ layers and stacks of four (n=4) perovskite unit cells $[Bi_3FeTi_3O_{13}]^{2-}$. The B-site polar distortions in the

ABO_3-type perovskite layers, confined within the a-c plane of the Aurivillius crystal, govern the final polarization state in BFTO.[21,26] The out-of-plane polarization components of the perovskite blocks adopt an anti-polar ordering with the polarization being attracted towards the nearest Bi_2O_2 layer and leading to a vanishing net out-of-plane polarization. The in-plane components, in contrast, align along a single direction, giving rise to the uniaxial in-plane ferroelectricity in BFTO, parallel to the a-lattice parameter.[24,27,28] In order to investigate how OPBs affect the polar order in the films, we use density functional theory (DFT) calculations for which we construct a unit cell made up of 384 atoms and comprising one OPB, shown in Figure 1a.

We start by examining changes in the electric dipole configuration, triggered by a shift in the BFTO crystal lattice equivalent to a perovskite unit-cell height in the [001] vertical direction, i.e., along the out-of-plane *c*-axis (Fig. 1a). Figure 1b shows the calculated local *B*-site polar displacements in the *a*-*c* plane around the created OPB. While the out-of-plane components adjust to match the anti-polar ordering of the neighboring unit cells on the other side of OPB, the orientation of the *a*-oriented net in-plane polarization component remains unchanged across the OPB, as shown in Figure 1b. We note that the right-pointing in-plane polarization direction is chosen arbitrarily, as both directions along the *a*-axis are equivalent by symmetry. This suggests that the sole consideration of structural changes and their influence on the local arrangement of electric dipoles cannot fully reproduce the experimentally reported reorientation of the net polarization at OPBs.[21,22]

A careful analysis of the atomic structure at the OPB reveals a significant mismatch in bonding between the adjacent BFTO unit cells, see Figure 1a. In particular, we observe large octahedral

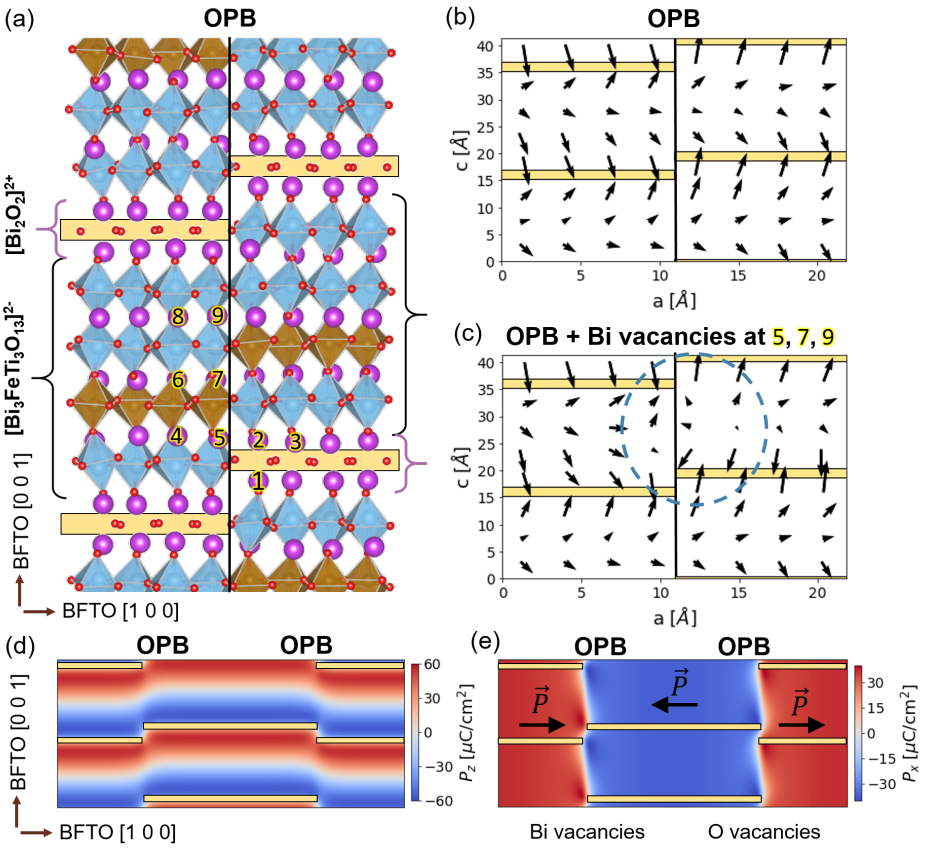

Figure 1. Theoretical model of in-plane polarization reversal at OPBs in Aurivillius BFTO thin films. (a) Atomic structure of BFTO lattice at the OPB calculated with DFT. The numbers correspond to the defect sites analyzed. An *inner* distribution of Fe ions is implemented (brown polyhedra) as it is the lowest energy configuration.[29] Yellow bars correspond to the negatively charged oxygen layers. (b) Local off-centering of the Fe/Ti ions around the OPB calculated with DFT. (c) Local polarization reversal demonstrated with DFT for defects at sites 5, 7, and 9. (d,e) Phase-field simulation of the out-of-plane (d) and the in-plane (e) polarization components across two OPBs with localized negatively and positively charged vacancies that stabilize HH and TT domain walls, respectively.

distortions due to the strain gradient at the interfaces between the Bi_2O_2 fluorite-like layer and the perovskite layer between the two adjacent BFTO unit cells at the OPB. The Bi-Bi bond length is considerably shorter in Bi_2O_2 layers compared to the perovskite one. Such strain gradients in the crystal lattice can be relieved by the creation of cationic or oxygen vacancies.[30] The Bi volatility[31–33] motivates us to quantify the formation energies of Bi off-stoichiometry, i.e. Bi vacancies,

at the OPB sites (marked 1 to 9 in Figure 1a) using DFT calculations. Indeed, our calculations reveal that the preferred Bi vacancy sites belong to the highly-strained Bi_2O_2-perovskite interface, see Figure S1 in the Supporting Information. Since off-stoichiometry can impact polarization,[34,35] we now look at how the pattern of local *B*-site off-centering around the OPB is affected when Bi atoms are removed from sites 5, 7, and 9, see Figure 1c. A local polarization reversal and, hence, a polar pattern similar to a HH wall is observed around the vacancy site (the dashed circle indicates the location of the electric-dipole reorientation in Figure 1c). This is in agreement with a previous report of oxygen off-stoichiometry-driven stabilization of TT walls in $BaTiO_3$.[36] A similar mechanism of non-stoichiometric defects stabilizing charged domain boundaries has recently been reported for an improper ferroelectric of Ruddlesden-Popper phase, in which the excess ions accumulate at charged TT domain walls.[22]

Our calculations suggest that the combination of structural changes and Bi vacancies at OPBs promotes the nucleation of HH domain walls in BFTO films. To maintain the charge neutrality in BFTO films, the creation of negatively charged oxygen vacancies is also expected owing to loss of Bi_2O_3 during the film processing.[37] Such defects are most likely stabilizing the TT domain-wall type at the OPBs. While DFT calculations are well suited to calculate the changes in the local structure, the complexity of the BFTO unit cell limits the length scale of our DFT studies. In order to predict the evolution of the polarization across the OPBs on larger length scales, we use a simple electrostatic phase-field model based on experimental values, considering both positively- and negatively-charged defects (for more details about the model see Supporting Information Supplementary note 2). Our model reproduces the anti-polar ordering along the c-axis (Fig. 1d) and, most

importantly, demonstrates that a full macroscopic reversal of in-plane polarization is stabilized at the OPBs (Fig. 1e).

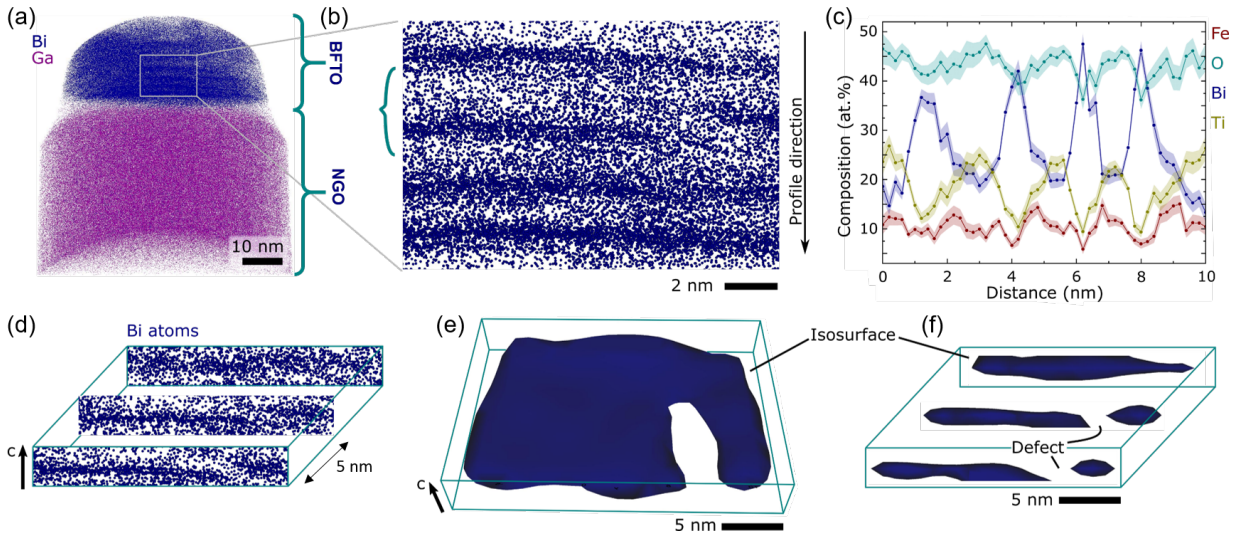

Figure 2. Atomic scale characterization of OPBs using APT. (a) Three-dimensional reconstruction of the full needle volume showing the thin film on top and the NGO substrate below (only Bi and Ga atoms are shown). (b) The central part of the needle volume shows the Bi-rich layers, including one growth defect in the top-right. (c) Compositional profile from the volume shown in (b). (d) Three slices from the defect-volume in (b) from the region of the green marker showing the evolution of the structural defect through the volume. (e), (f) Isosurfaces around the OPB containing a high Bi-density. The vacant part on the right corresponds to the OPB.

Let us now investigate the OPB formation in our ultrathin BFTO n=4 films. The films of the Aurivillius phase are grown using PLD with reflection high energy electron diffraction (RHEED) monitoring to ensure the sub-unit-cell thickness accuracy.[38,39] The excellent epitaxial lattice matching between BFTO and NGO (001) (henceforth crystallographic indices correspond to the orthorhombic u.c. notation) substrate results in films that are single-crystalline and uniaxially polarized along the [010] substrate direction (a-axis of BFTO).[38,39] We use APT to image a 5-u.c.-thick BFTO film. The APT measurement allows three-dimensional reconstruction of the chemical composition on the atomic length scale and helps to locate structural defects and their

propagation within the volume.[40] For this purpose, a needle-shaped specimen is prepared from the BFTO thin film using a focused ion beam (see Experimental section). Figure 2a shows the three-dimensional reconstruction of the full needle volume with a sharp interface between the film and the substrate. The distribution of Ga atoms represents the NGO substrate, whereas Bi atoms are selected to illustrate the structure of the BFTO film grown on top. Figure 2b shows a map of Bi atoms in the central part of the needle, which corresponds to the thickness of approximately 2 u.c. The Bi-rich layers allow a direct identification of flourite-like $[Bi_2O_2]^{2+}$ planes. The second flourite-like layer (marked in Fig. 2b) contains an apparent translational shift, which highlights the location of the OPB. Elemental analysis around the defect reveals that the Bi-rich layers are not directly overlapping, but instead terminate some distance away from their expected meeting point at the OPB. This suggests that the Bi_2O_2 layers are depleted in Bi, confirming the cation vacancy formation right at the OPB, in line with the DFT calculations. The corresponding integrated compositional profile of the volume along the direction indicated in Figure 2b is given in Figure 2c. In contrast to previous cross-sectional STEM studies,[16,21,26] APT provides us with full three-dimensional information. By investigating multiple slices of the identified structural defect (Fig. 2d) we find that the OPB propagates into the film depth. The vacant parts of the Bi-density isosurfaces shown in Figure 2e,f correspond to the OPB and reveal that the defect is relatively straight and stretches for at least 10 nm into the film volume, defining it as a quasi-1D defect. The analysis of the distribution of Bi atoms across the OPB reveals a reduction in Bi concentration by 5.4 ± 3.0 at. % at the OPB relative to the bulk of the specimen (Supporting Information Fig. S3). Additionally, the mass spectrum acquired from the full film volume reveals a non-stoichiometry of

Bi and O elements (Supporting Information Fig. S4). Thus, as suggested by our DFT calculations, the APT data corroborate the emergence of an optimal setting for the stabilization of ferroelectric domain walls at the OPB.

The OPB we investigated by APT is isolated and formed spontaneously in the bulk of the film.[39] To trigger the deterministic nucleation of 1D defects, we take advantage of the out-of-plane lattice parameter mismatch between the BFTO film and the substrate.[38] From one NGO substrate terrace to the other, the BFTO unit cells grown on top are shifted by a fraction of the unit cell in the vertical direction, leading to the formation of so-called steric OPBs at every substrate step[16,41,42] as shown in the sketch in Figure 3a. This approach of creating structural defects is highly deterministic and versatile, as both the substrate step density and their shape can be tuned by the substrate preparation and its miscut angle selection (Fig. 3b). We start by investigating the correlation between the topography and the ferroelectric domain distribution in ultrathin epitaxial BFTO ferroelectric films using a combination of atomic force microscopy (AFM) and PFM prior to and post-deposition of the ferroelectric films, respectively. Figure 3c shows the topography of an as-received NGO (001) substrate (ca. 0.02° miscut) with its terraces of variable width arranged in a random fashion. After deposition of 1 u.c ($\sim$4 nm)-thick BFTO film, the room temperature lateral PFM was performed (Fig. 3d). The PFM signal reveals a ferroelectric domain patternshowing a close resemblance to the substrate terrace morphology.

The striking similarity between the substrate topography and the domain pattern points to steric OPBs as the most probable origin of the domain nucleation in our films as suggested by our

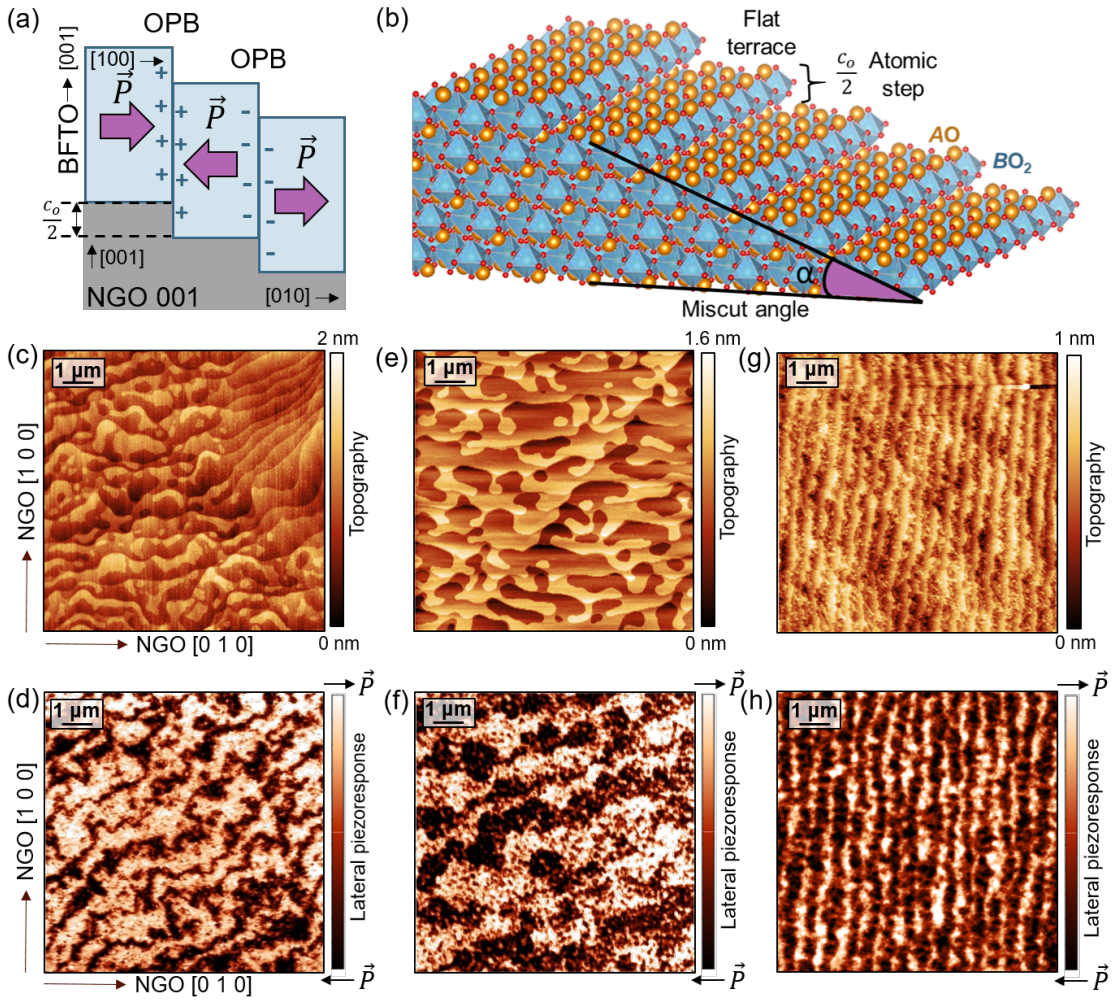

Figure 3. Ferroelectric domain engineering using a controlled formation of steric OPBs. (a) Schematic depicting OPB formation in BFTO at every substrate step, leading to the nucleation of ferroelectric domain walls. (b) Schematic of atomically flat terraces and substrate steps of a perovskite-type ABO_3 crystal. Topography of NGO (001) substrate with a 0.02° miscut angle (c) and the corresponding domain configuration in 1 u.c.-thick BFTO grown onto it (d). Topography of annealed NGO (001) substrate (0.02° miscut angle) (e) and resulting domains in 1 u.c.-thick BFTO (f). Topography of NGO (001) substrate with a higher miscut angle of 0.05° (g), leading to aligned narrow terraces that translate into stripe domains in 1 u.c.-thick BFTO (h).

DFT calculations (Fig. 1). The altered chemical environment of OPBs, namely Bi and O vacancies (Fig. 2c), stabilizes the domain wall formation. The uniaxial nature of single-crystalline BFTO film reduces the allowed domain variants and leads to periodically arranged HH and TT charged

domain walls with the in-plane polarization reversal of 180°[38,39] at every substrate step, running perpendicular to the polar axis of the film. The correlation between the substrate morphology and the domain pattern opens up new avenues for defining the exact location, shape of domain walls and even tuning the size of domains, which we now demonstrate by varying the means of substrate preparation and its miscut angle α. Substrate annealing or chemical etching influences the shape of step edges, while the miscut angle impacts the spacing between the step terraces.[43] Figure 3e shows the AFM image of the NGO substrate topography (0.02° miscut) after additional thermal annealing at 1200°C in oxygen atmosphere, which leads to larger substrate terraces that directly translate into wider ferroelectric domains (Fig. 3f). Figure 3g shows the topography of the NGO substrate with a higher 0.05° miscut angle, which gives rise to straight, short-period step edges. As anticipated, the LPFM scan recorded on 1 u.c.-thick BFTO layers deposited on this template reveals straight and closely packed stripe domains (Fig. 3h), proving the effectiveness and tunability of the domain formation driven by steric OPBs. Lastly, we note that it is important to consider the direction of the substrate miscut for the nucleation of domains. As our Aurivillius thin films exhibit a uniaxial in-plane-polarization along the [010] substrate direction,[38,39] off-stoichiometry at steric OPBs induced by substrate miscut along the orthogonal direction is not expected to affect the polarization state as no charged domain walls could form in that geometry.

Domain engineering via ordering of OPBs is highly effective in ultrathin films of the Aurivillius phase, in which structural constraints play a decisive role. Upon the increase in film thickness, the weak interlayer coupling and increasing electrostatic energy of charged domain walls, however, render the domain ordering challenging.[44] In our films, we see that upon increasing the BFTO

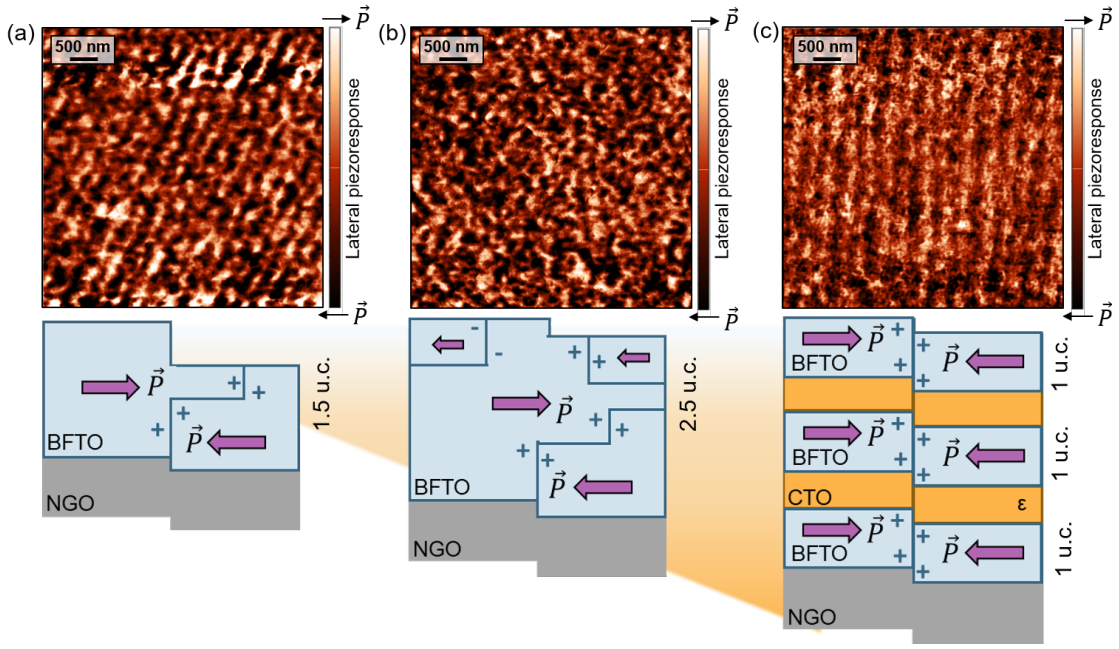

Figure 4. Robustness of domain engineering in heterostructures. (a) LPFM image of 1.5 u.c. of BFTO grown directly on NGO. (b) LPFM image of 2.5 u.c. of BFTO grown directly on NGO. (c) LPFM image of a (BFTO|CTO)$_2$|BFTO multilayer, with 1 u.c. of BFTO and 4 u.c. of CTO as the repeat unit. The strong piezoresponse of the multilayer suggests a parallel alignment of the polarization within each of the three BFTO layers. Note that the off-stoichiometry (i.e., Bi- or O-vacancies) at the OPB is most likely preserved throughout the thickness of the film. This maintains the polarization direction in each layer and stabilize the same type of domain wall (i.e., HH or TT).

thickness by just one half-unit cell, the stripe domain pattern gets altered: stripes start to merge, in this way creating neutral (side-by-side) domain walls instead of the charged ones (Fig. 4a). This is consistent with the increasing electrostatic cost of maintaining charged domain walls with increasing film volume. At an even higher thickness of 2.5 u.c. of BFTO (Fig. 4b), the stripe domain pattern gets completely lost and the randomly oriented small in-plane domains prevail leading to a significant reduction of electrostatic costs.

In order to combat this loss of substrate step imprint in the domain pattern, we now consider a dielectric|ferroelectric multilayer. The lattice-matched $CaTiO_3$ (CTO) dielectric spacers propagate

the OPBs, while isolating ferroelectric BFTO layers from each other. This prevents the build-up of electrostatic potential and domain disorder despite the increasing thickness. Figure 4c shows a PFM image of the domain configuration in the (BFTO|CTO)$_2$|BFTO|NGO superlattice. The characteristic HH and TT charged-domain-wall ordering of a single BFTO layer is maintained. We note that previous investigations of very thick ($>$ 30 nm) ferroelectric films of the Aurivillius phase demonstrated the OPB propagation through the thickness with a tilt away from the surface normal.[16,45] Here, however, we only consider a multilayer consisting of 1 unit-cell-thick Aurivillius building blocks. Hence, such tilt can be neglected and we can expect the width of each domain to be maintained. We thus establish a route to enforce domain ordering in ferroelectrics with full control over the domain wall shape and location as well as the domain size throughout the multilayer volume.

In summary, we introduce a new route to ferroelectric domain engineering via the ordering of structural defects. We identify OPBs as nucleation sites for ferroelectric domain walls on the basis of the altered bonding environment and susceptibility to non-stoichiometric defects that they exhibit. In line with this and consistent with our DFT calculations and phase-field simulations, APT identifies OPBs as 1D line defects with distinct changes in their chemical environment. We use this knowledge to define a domain pattern through substrate steps in ultrathin layered ferroelectrics of the Aurivillius phase. Going beyond commonly used methods for tuning ferroic domain configurations, we demonstrate full control over the domain size, shape, and location by merely tuning the substrate morphology. While our proposed approach is most effective in ultrathin layers, it can be extended to coherently strained dielectric|ferroelectric multilayers. We note that ferroelectric do-

main engineering through OPBs is applicable not only to other classes of layered ferroelectrics[25] such as the Dion-Jacobson[46] or Ruddlesden-Popper[47] phases, but also to classical pseudocubic perovskite ferroelectrics if they are deposited on crystal substrates that have different out-of-plane lattice parameters.[42]

Experimental section

Density-functional Theory Calculations Density functional theory calculations were performed using the VASP software package[48–51] using the PBEsol+U[52–54] functional. We construct the OPBs using supercells of size $4\times1\times1$ (384 atoms). We use a plane wave cutoff of 600 eV, and a k-point grid of $1\times2\times1$. Relaxations are done up to a threshold force of 0.1 eV/$\mathring{A}$ on each atom. We adopt an anti-ferromagnetic ordering of the Fe spins, and we apply a U of 3 eV on the Fe d-orbitals.

Phase-field model Phase-field calculations were carried out using a simple Landau model for spontaneous polarization in the pseudoperovskite units in combination with the electrostatic Poisson equation. The parameters were fit to match experimental values. We assume a strong negative charge in the O^{2-} layers and a compensating charge equally distributed over the rest of the BFTO unit cell. See Supporting Information Supplementary Note 2 for an exact description of the model and parameters used. The resulting phase-field equations were solved using finite volume methods as implemented in the Fipy software package.[55]

Thin-Film Growth BFTO films were grown by pulsed laser deposition at a substrate temperature of 700°C. Optimal oxygen partial pressure was found to be $1.5\cdot10^{-2}$ mbar. The KrF excimer laser intensity was set to 0.9 J cm^{-2}. The thickness of the films monitored with RHEED[38,39] was

additionally confirmed with X-ray reflectivity (XRR) measurements.

Atom Probe Tomography APT measurements were done with a Cameca LEAP 5000XS, operating in laser pulsing mode. Pulse energy was set to 60 pJ and the pulsing frequency was 250 kHz. During analysis the specimen was cooled down to 80K. Detection rate was set to 0.5%, meaning that on average 5 atoms were evaporated every 1000 pulses. Data analysis was done using Cameca IVAS 3.6.12. Samples for APT measurements were prepared using a Thermo Fisher Scientific G4 DualBeam UX Focused Ion Beam (FIB), following the steps described elsewhere.[56] See Supporting Information Fig. S5 for details on sample preparation.

Scanning Probe Microscopy The piezoresponse force microscopy acquisition was performed using a 5 V peak-to-peak AC modulation at 70 kHz in contact mode using a NT-MDT NTEGRA Prima scanning probe microscope. Images of in-plane polarized domains were recorded via cantilever torsion mode when measuring with cantilever perpendicular to the uniaxial polarization axis, respectively.[39,57]

X-ray diffraction The crystalline structure of thin films was analyzed by X-ray diffraction and reciprocal space mapping measurements using four-circle X-ray diffractometer (Panalytical X' Pert MRD).

Acknowledgements

E.G. and M.T. acknowledge the Swiss National Science Foundation under Project No. 200021_-188414. D.M. and K.A.H. acknowledge support the Research Council of Norway for support to the Norwegian Micro- and Nano-Fabrication Facility, NorFab, project number 245963/F50 and direct financial support by the Department of Materials Science and Engineering at NTNU.

D.M. acknowledges funding from the European Research Council (ERC) under the European Union's Horizon 2020 research and innovation program (Grant Agreement No. 863691) and further thanks NTNU for support through the Onsager Fellowship Program and NTNU's Outstanding Academic Fellows Program. Q.N.M. acknowledges support by the Swiss National Science Foundation under project No. P2EZP2_191872. Computational resources were provided by CEA Grenoble. Constantinos Hatzoglou is acknowledged for his support concerning the APT work at NTNU.

Author Contributions

All authors discussed the results. E.G. wrote the manuscript with M.T.. E.G. performed the thin-film growth, the scanning probe microscopy measurements, and the structural analysis of the films. K.A.H. performed atom probe tomography supervised by D.M.. Q.N.M. performed the DFT calculations and phase-field simulations. M.T. designed the experiment together with E.G. and supervised the work jointly with D.M.

Notes

The authors declare that they have no competing financial interests.

Keywords:

ferroelectric domains, charged domain walls, ultrathin ferroelectrics, out-of-phase boundaries, layered Aurivillius ferroelectrics.

Supporting information available:

Bi vacancy formation energies around OPB, model for phase-field simulations of ferroelectric behavior at OPBs, APT-based analysis of Bi content, mass spectrum of BFTO film, details on

sample preparation for APT analysis.

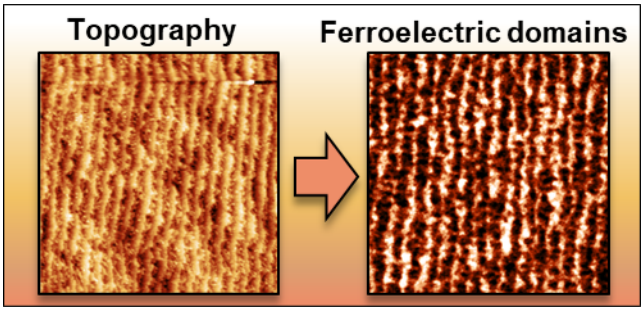

Table of contents figure.

References

1. Matzen, S.; Fusil, S. Domains and domain walls in multiferroics. *Comptes Rendus Physique* **2015**, *16*, 227–240.

2. Strkalj, N.; Gradauskaite, E.; Nordlander, J.; Trassin, M. Design and manipulation of ferroic domains in complex oxide heterostructures. *Materials* **2019**, *12*, 3108.

3. Meier, D.; Selbach, S. M. Ferroelectric domain walls for nanotechnology. *Nature Reviews Materials* **2022**, *7*, 157–173.

4. Chanthbouala, A.; Garcia, V.; Cherifi, R. O.; Bouzehouane, K.; Fusil, S.; Moya, X.; Xavier, S.; Yamada, H.; Deranlot, C.; Mathur, N. D.; Bibes, M.; Barthélémy, A.; Grollier, J. A ferroelectric memristor. *Nature Materials* **2012**, *11*, 860–864.

5. Kim, D. J.; Lu, H.; Ryu, S.; Bark, C. W.; Eom, C. B.; Tsymbal, E. Y.; Gruverman, A. Ferroelectric tunnel memristor. *Nano Letters* **2012**, *12*, 5697–5702.

6. Sharma, P.; Zhang, Q.; Sando, D.; Lei, C. H.; Liu, Y.; Li, J.; Nagarajan, V.; Seidel, J. Nonvolatile ferroelectric domain wall memory. *Science Advances* **2017**, *3*, e1700512.

7. Sharma, P.; Sando, D.; Zhang, Q.; Cheng, X.; Prosandeev, S.; Bulanadi, R.; Prokhorenko, S.; Bellaiche, L.; Chen, L. Q.; Nagarajan, V.; Seidel, J. Conformational Domain Wall Switch. *Advanced Functional Materials* **2019**, *29*, 1807523.

8. Seidel, J. et al. Conduction at domain walls in oxide multiferroics. *Nature Materials* **2009**, *8*,

229–234.

9. Meier, D.; Seidel, J.; Cano, A.; Delaney, K.; Kumagai, Y.; Mostovoy, M.; Spaldin, N. A.; Ramesh, R.; Fiebig, M. Anisotropic conductance at improper ferroelectric domain walls. *Nature Materials* **2012**, *11*, 284–288.

10. Whyte, J. R.; Gregg, J. M. A diode for ferroelectric domain-wall motion. *Nature Communications* **2015**, *6*, 7361.

11. Schlom, D. G.; Chen, L. Q.; Eom, C. B.; Rabe, K. M.; Streiffer, S. K.; Triscone, J. M. Strain tuning of ferroelectric thin films. *Annual Review of Materials Research* **2007**, *37*, 589–626.

12. Gradauskaite, E.; Meisenheimer, P.; Müller, M.; Heron, J.; Trassin, M. Multiferroic heterostructures for spintronics. *Physical Sciences Reviews* **2021**, *6*, 20190072.

13. Feigl, L.; Yudin, P.; Stolichnov, I.; Sluka, T.; Shapovalov, K.; Mtebwa, M.; Sandu, C. S.; Wei, X. K.; Tagantsev, A. K.; Setter, N. Controlled stripes of ultrafine ferroelectric domains. *Nature Communications* **2014**, *5*, 4677.

14. Sarott, M. F.; Fiebig, M.; Trassin, M. Tracking ferroelectric domain formation during epitaxial growth of $PbTiO_3$ films. *Applied Physics Letters* **2020**, *117*, 132901.

15. De Luca, G.; Rossell, M. D.; Schaab, J.; Viart, N.; Fiebig, M.; Trassin, M. Domain Wall Architecture in Tetragonal Ferroelectric Thin Films. *Advanced Materials* **2017**, *29*, 1605145.

16. Zurbuchen, M. A.; Tian, W.; Pan, X. Q.; Fong, D.; Streiffer, S. K.; Hawley, M. E.; Lettieri, J.; Jia, Y.; Asayama, G.; Fulk, S. J.; Comstock, D. J.; Knapp, S.; Carim, A. H.; Schlom, D. G. Morphology, structure, and nucleation of out-of-phase boundaries (OPBs) in epitaxial films of layered oxides. *Journal of Materials Research* **2007**, *22*, 1439–1471.

17. Deepak, N.; Carolan, P.; Keeney, L.; Pemble, M. E.; Whatmore, R. W. Tunable nanoscale structural disorder in Aurivillius phase, $n = 3$ $Bi_4Ti_3O_{12}$ thin films and their role in the transformation to $n = 4$... *Journal of Materials Chemistry C* **2015**, *3*, 5727–5732.

18. Wei, X. K.; Tagantsev, A. K.; Kvasov, A.; Roleder, K.; Jia, C. L.; Setter, N. Ferroelectric translational antiphase boundaries in nonpolar materials. *Nature Communications* **2014**, *5*, 3031.

19. Zhang, Y.; Han, M. G.; Sando, D.; Wu, L.; Valanoor, N.; Zhu, Y. Antiphase-Boundary-Engineered Domain Switching in a (110)-Oriented $BiFeO_3$ Film. *ACS Applied Electronic Materials* **2021**, *3*, 3226–3233.

20. Kim, J. et al. Superconducting Sr_2RuO_4 Thin Films without Out-of-Phase Boundaries by Higher-Order Ruddlesden-Popper Intergrowth. *Nano Letters* **2021**, *21*, 4185–4192.

21. Moore, K.; O'Connell, E. N.; Griffin, S. M.; Downing, C.; Colfer, L.; Schmidt, M.; Nicolosi, V.; Bangert, U.; Keeney, L.; Conroy, M. Charged Domain Wall and Polar Vortex Topologies in a Room-Temperature Magnetoelectric Multiferroic Thin Film. *ACS Applied Materials Interfaces* **2022**, *14*, 5525–5536.

22. Nakajima, H.; Kurushima, K.; Mine, S.; Tsukasaki, H.; Matsuoka, M.; Gao, B.; Cheong, S.-W.; Mori, S. Charged domain boundaries stabilized by translational symmetry breaking in the hybrid improper ferroelectric $Ca_{3-x}Sr_xTi_2O_7$. *Communications Materials* **2021**, *2*, 109.

23. Aurivillius, B. Mixed Bismuth Oxides with Layer Lattices. 1. The Structure Type of $CaNb_2Bi_2O_9$. *Arkiv. Kemi.* **1949**, *1*, 463–480.

24. Newnham, R. E.; Wolfe, R. W.; Dorrian, J. F. Structural basis of ferroelectricity in the bismuth titanate family. *Materials Research Bulletin* **1971**, *6*, 1029–1039.

25. Benedek, N. A.; Rondinelli, J. M.; Djani, H.; Ghosez, P.; Lightfoot, P. Understanding ferroelectricity in layered perovskites: New ideas and insights from theory and experiments. *Dalton Transactions* **2015**, *44*, 10543–10558.

26. Campanini, M.; Trassin, M.; Ederer, C.; Erni, R.; Rossell, M. D. Buried In-Plane Ferroelectric Domains in Fe-Doped Single-Crystalline Aurivillius Thin Films. *ACS Applied Electronic Materials* **2019**, *1*, 1019–1028.

27. Hervoches, C. H.; Snedden, A.; Riggs, R.; Kilcoyne, S. H.; Manuel, P.; Lightfoot, P. Structural behavior of the four-layer aurivillius-phase ferroelectrics $SrBi_4Ti_4O_{15}$ and $Bi_5Ti_3FeO_{15}$. *Journal of Solid State Chemistry* **2002**, *164*, 280–291.

28. Funakubo, H. Degradation-free dielectric property using bismuth layer-structured dielectrics having natural superlattice structure. *Journal of the Ceramic Society of Japan* **2008**, *116*,

1249–1254.

29. Birenbaum, A. Y.; Ederer, C. Potentially multiferroic Aurivillius phase $Bi_5FeTi_3O_{15}$: Cation site preference, electric polarization, and magnetic coupling from first principles. *Physical Review B* **2014**, *90*, 214109.

30. Aschauer, U.; Pfenninger, R.; Selbach, S. M.; Grande, T.; Spaldin, N. A. Strain-controlled oxygen vacancy formation and ordering in $CaMnO_3$. *Physical Review B - Condensed Matter and Materials Physics* **2013**, *88*, 054111.

31. Alexe, M.; Scott, J. F.; Curran, C.; Zakharov, N. D.; Hesse, D.; Pignolet, A. Self-patterning nano-electrodes on ferroelectric thin films for gigabit memory applications. *Applied Physics Letters* **1998**, *73*, 1592–1594.

32. Béa, H.; Bibes, M.; Barthélémy, A.; Bouzehouane, K.; Jacquet, E.; Khodan, A.; Contour, J. P.; Fusil, S.; Wyczisk, F.; Forget, A.; Lebeugle, D.; Colson, D.; Viret, M. Influence of parasitic phases on the properties of $BiFeO_3$ epitaxial thin films. *Applied Physics Letters* **2005**, *87*, 3–5.

33. Liao, Z.; Brahlek, M.; Ok, J. M.; Nuckols, L.; Sharma, Y.; Lu, Q.; Zhang, Y.; Lee, H. N. Pulsed-laser epitaxy of topological insulator Bi_2Te_3 thin films. *APL Materials* **2019**, *7*, 041101.

34. Park, C.; Chadi, D. Microscopic study of oxygen-vacancy defects in ferroelectric per-

ovskites. *Physical Review B - Condensed Matter and Materials Physics* **1998**, *57*, R13961.

35. Scott, J. F.; Dawber, M. Oxygen-vacancy ordering as a fatigue mechanism in perovskite ferroelectrics. *Applied Physics Letters* **2000**, *76*, 3801.

36. Petralanda, U.; Kruse, M.; Simons, H.; Olsen, T. Oxygen Vacancies Nucleate Charged Domain Walls in Ferroelectrics. *Physical Review Letters* **2021**, *127*, 117601.

37. Li, M.; Pietrowski, M. J.; De Souza, R. A.; Zhang, H.; Reaney, I. M.; Cook, S. N.; Kilner, J. A.; Sinclair, D. C. A family of oxide ion conductors based on the ferroelectric perovskite $Na_{0.5}Bi_{0.5}TiO_3$. *Nature Materials* **2014**, *13*, 31–35.

38. Gradauskaite, E.; Campanini, M.; Biswas, B.; Schneider, C. W.; Fiebig, M.; Rossell, M. D.; Trassin, M. Robust In-Plane Ferroelectricity in Ultrathin Epitaxial Aurivillius Films. *Advanced Materials Interfaces* **2020**, *7*, 2000202.

39. Gradauskaite, E.; Gray, N.; Campanini, M.; Rossell, M. D.; Trassin, M. Nanoscale Design of High-Quality Epitaxial Aurivillius Thin Films. *Chemistry of Materials* **2021**, *33*, 9439–9446.

40. Gault, B.; Chiaramonti, A.; Cojocaru-Mirédin, O.; Stender, P.; Dubosq, R.; Freysoldt, C.; Makineni, S. K.; Li, T.; Moody, M.; Cairney, J. M. Atom probe tomography. *Nature Reviews Methods Primers* **2021**, *1*, 51.

41. Jiang, J. C.; Lin, Y.; Chen, C. L.; Chu, C. W.; Meletis, E. I. Microstructures and surface step-

induced antiphase boundaries in epitaxial ferroelectric $Ba_{0.6}Sr_{0.4}TiO_3$ thin film on MgO. *Journal of Applied Physics* **2002**, *91*, 3188–3192.

42. Wang, Z.; Guo, H.; Shao, S.; Saghayezhian, M.; Li, J.; Fittipaldi, R.; Vecchione, A.; Siwakoti, P.; Zhu, Y.; Zhang, J.; Plummer, E. W. Designing antiphase boundaries by atomic control of heterointerfaces. *Proceedings of the National Academy of Sciences of the United States of America* **2018**, *115*, 9485–9490.

43. Sánchez, F.; Ocal, C.; Fontcuberta, J. Tailored surfaces of perovskite oxide substrates for conducted growth of thin films. *Chemical Society Reviews* **2014**, *43*, 2272–2285.

44. Zurbuchen, M. A.; Asayama, G.; Schlom, D. G.; Streiffer, S. K. Ferroelectric Domain Structure of $SrBi_2Nb_2O_9$ Epitaxial Thin Films. *Physical Review Letters* **2002**, *88*, 107601.

45. Deepak, N.; Zhang, P. F.; Keeney, L.; Pemble, M. E.; Whatmore, R. W. Atomic vapor deposition of bismuth titanate thin films. *Journal of Applied Physics* **2013**, *113*, 187207.

46. Jacobson, A. J.; Johnson, J. W.; Lewandowski, J. T. Interlayer Chemistry between Thick Transition-Metal Oxide Layers: Synthesis and Intercalation Reactions of $K[Ca_2Na_{n-3}Nb_nO_{3n+1}]$ (3 n 7). *Inorganic Chemistry* **1985**, *24*, 3727–3729.

47. Ruddlesden, S. N.; Popper, P. New compounds of the K_2NIF_4 type. *Acta Crystallographica* **1957**, *10*, 538–539.

48. Kresse, G.; Hafner, J. Ab initio molecular dynamics for liquid metals. *Physical Review B -*

Condensed Matter and Materials Physics **1993**, *47*, 558–561.

49. Kresse, G.; Hafner, J. Ab initio molecular-dynamics simulation of the liquid-metal–amorphous-semiconductor transition in germanium. *Physical Review B - Condensed Matter and Materials Physics* **1994**, *49*, 14251–14269.

50. Kresse, G.; Furthmüller, J. Efficiency of ab-initio total energy calculations for metals and semiconductors using a plane-wave basis set. *Comput. Mater. Sci.* **1996**, *6*, 15–50.

51. Kresse, G.; Furthmüller, J. Efficient iterative schemes for ab initio total-energy calculations using a plane-wave basis set. *Physical Review B - Condensed Matter and Materials Physics* **1996**, *54*, 11169–11186.

52. Perdew, J. P.; Burke, K.; Ernzerhof, M. Generalized Gradient Approximation Made Simple. *Physical Review Letters* **1996**, *77*, 3865–3868.

53. Perdew, J. P.; Ruzsinszky, A.; Csonka, G. I.; Vydrov, O. A.; Scuseria, G. E.; Constantin, L. A.; Zhou, X.; Burke, K. Restoring the Density-Gradient Expansion for Exchange in Solids and Surfaces. *Physical Review Letters* **2008**, *100*, 136406.

54. Liechtenstein, A. I.; Anisimov, V. I.; Zaanen, J. Density-functional theory and strong interactions: Orbital ordering in Mott-Hubbard insulators. *Physical Review B - Condensed Matter and Materials Physics* **1995**, *52*, R5467–R5470.

55. Guyer, J. E.; Wheeler, D.; Warren, J. A. FiPy: Partial Differential Equations with Python.

Comput. Sci. Eng. **2009**, *11*, 6–15.

56. Thompson, K.; Lawrence, D.; Larson, D. J.; Olson, J. D.; Kelly, T. F.; Gorman, B. In situ site-specific specimen preparation for atom probe tomography. *Ultramicroscopy* **2007**, *107*, 131–139.

57. Keeney, L.; Colfer, L.; Schmidt, M. Probing Ferroelectric Behavior in Sub-10 nm Bismuth-Rich Aurivillius Films by Piezoresponse Force Microscopy. *Microscopy and Microanalysis* **2021**, *doi:10.101*, 1–11.